

Journal of Geophysical Research: Earth Surface

RESEARCH ARTICLE

10.1002/2014JF003349

Key Points:

- Submarine groundwater discharge introduces freshwater into marine sediments
- Fresh pore water preserves submarine permafrost and favors gas hydrate stability
- Today's submarine permafrost extent relates to groundwater discharge strength

Correspondence to:J. M. Frederick,
jenn@dri.edu**Citation:**

Frederick, J. M., and B. A. Buffett (2015), Effects of submarine groundwater discharge on the present-day extent of relict submarine permafrost and gas hydrate stability on the Beaufort Sea continental shelf, *J. Geophys. Res. Earth Surf.*, 120, 417–432, doi:10.1002/2014JF003349.

Received 23 SEP 2014

Accepted 31 JAN 2015

Accepted article online 9 FEB 2015

Published online 11 MAR 2015

Effects of submarine groundwater discharge on the present-day extent of relict submarine permafrost and gas hydrate stability on the Beaufort Sea continental shelf

J. M. Frederick¹ and B. A. Buffett²

¹Division of Hydrologic Sciences, Desert Research Institute, Reno, Nevada, USA, ²Department of Earth and Planetary Science, University of California, Berkeley, California, USA

Abstract We investigate the role of submarine groundwater discharge on the offshore temperature and salinity field and its effect on the present-day extent of submarine permafrost and gas hydrate stability on the North American Beaufort Shelf with a two-dimensional numerical model based on the finite volume method. This study finds that submarine groundwater discharge can play a large role in submarine permafrost evolution and gas hydrate stability, suggesting that local hydrology may control the evolution of submarine permafrost as strongly as does sea level or paleoclimatic conditions. Submarine permafrost evolution shows transient behavior over potentially long time scales (e.g., several glacial cycles) before a balance of density- and pressure-driven flows is established with the permeability variations imposed by the overlying permafrost layer. The “detectable” offshore permafrost extent is related to the quasi-stationary location of the saltwater-freshwater transition. Larger values of submarine groundwater discharge allow permafrost to extend farther offshore because fresh pore water preserves relict ice. Therefore, differences in the permafrost extent at locations that share similar paleoclimatic history may be explained in part by differences in the local hydrology. Gas hydrate stability on the North American Beaufort Shelf may be more widespread than currently thought because low-ice saturation, highly degraded submarine permafrost likely exists beyond the boundary detectable by common geophysical methods.

1. Introduction

Methane hydrate is an ice-like solid that can sequester large quantities of methane gas in marine sediments along most continental margins where thermodynamic conditions permit its formation. Along the circum-Arctic shelf, relict permafrost-associated methane hydrate deposits formed when nonglaciated portions of the shelf experienced subaerial exposure during ocean transgressions [Collett, 1994]. While the Arctic methane hydrate reservoir is thought to be small compared to deepwater deposits along non-Arctic margins, it is postulated that contemporary and future gas hydrate degradation will primarily occur in the Arctic [Ruppel, 2011]. Degradation of this shallow-water reservoir has the potential to release large quantities of methane gas as ocean inundation continues to warm permafrost- and hydrate-bearing sediments in the Arctic [Frederick and Buffett, 2014].

Gas hydrate stability and the permeability of circum-Arctic shelf sediments to gas migration are closely linked with relict submarine permafrost. Submarine permafrost extent depends on several environmental factors. The shelf lithology, sea level variations, mean annual air temperature, ocean bottom water temperature, geothermal heat flux, groundwater hydrology, and the salinity of the pore water are all important controls, to name a few [Osterkamp, 2001]. The salinity of the pore water partially controls the freezing point depression for both ice and gas hydrate. When marine sediments are first deposited, the pore fluid takes on the salinity of the depositional environment. The salinity of the pore water may evolve from the depositional environment in time by solute transport via advection or diffusion. For example, shallow drilling (< 65 m depth) near Prudhoe Bay, Alaska, revealed pore water salinity near seawater values [Sellmann and Chamberlain, 1980]; however, deeper well log data at the Canadian Beaufort Shelf indicate marine sediments between 200 and 2000 m depth are fresh [Weaver and Stuart, 1983]. Although it is unknown whether these sediments were originally fresh, a topographically driven submarine discharge of fresh terrestrial groundwater may explain deep offshore freshening (e.g., see reviews by Taniguchi *et al.*

[2002], Bratton [2010], Moore [2010], and Post *et al.* [2013]). Because submarine permafrost creates a relatively impermeable barrier to fluid movement, confinement imparts a sort of anisotropy to the shelf sediment system [Williams, 1970]. Fresh terrestrial groundwater discharge will tend to travel horizontally offshore beneath the submarine-confining unit (e.g., the impermeable permafrost layer), and a freshwater-saltwater interface is typically located where the fresh terrestrial groundwater discharge meets its seaward edge [Bratton, 2010]. However, in the case of relict submarine permafrost, the offshore extent of the confining unit evolves in time, making the location of the brackish mixing zone (and its feedback on submarine permafrost) difficult to predict without numerical techniques. While deep salinity measurements are scarce on the Arctic continental shelf (and direct measurements of groundwater flow do not exist), indirect methods, such as measurements of heat flow variation, imply significant groundwater movement both onshore and offshore [Deming *et al.*, 1992; Judge and Majorowicz, 1992].

Submarine groundwater discharge as a component of the hydrologic cycle has largely been ignored by the scientific community. Only recently have the vast global offshore groundwater reserves been given due attention [Taniguchi *et al.*, 2002; Post *et al.*, 2013], prompting new speculation on the relationship with marine gas hydrate deposits. The transport of mobile carbon in meteoric waters via submarine groundwater discharge is postulated as a global gas hydrate formation mechanism [Barenbaum, 2007], while variations in the submarine groundwater discharge are cited as a probable cause of gas hydrate dissociation and methane gas release in the Arctic [Dzyuba and Zektser, 2013]. Observations of vigorous gas plumes and methane venting from the circum-Arctic shelf sediments conceivably linked to permafrost and gas hydrate dissociation have recently been reported. For example, localized gas venting from a pingo-like feature on the Canadian Beaufort Shelf was measured at $\sim 5 \text{ L h}^{-1}$ in 2003 [Paull *et al.*, 2007] and was still venting methane when observed again in 2010 [Paull *et al.*, 2011]. Widespread gas flares have been observed in water depths $> 20 \text{ m}$ at the South Kara Sea, Russia [Portnov *et al.*, 2013], as well as near the Lena River Delta [Shakhova *et al.*, 2013]. Given the significant role that fluid flow plays in gas hydrate systems, the effect of submarine groundwater discharge on gas hydrate stability warrants closer attention.

Numerical models of submarine permafrost and gas hydrate stability are difficult to construct because field observations required for proper model validation are scarce [Judge *et al.*, 1981; Weaver and Stuart, 1983; Osterkamp *et al.*, 1989; Smith and Judge, 1993; Dallimore and Collett, 1995; Kassens *et al.*, 2000; Rachold *et al.*, 2007; Brothers *et al.*, 2012; Hu *et al.*, 2013]. Reproducing the present-day distribution of permafrost requires knowledge of paleoclimatic conditions, which inherently contains some level of uncertainty. As a result, numerically modeling submarine permafrost and gas hydrate stability requires some approximation. Early models of submarine permafrost and gas hydrate stability were one-dimensional for simplicity [e.g., Judge and Majorowicz, 1992; Taylor *et al.*, 1996a, 1996b], but more recent work [e.g., Delisle, 1998; Romanovskii *et al.*, 2005; Nicolsky and Shakhova, 2010; Nicolsky *et al.*, 2012; Taylor *et al.*, 2013; Portnov *et al.*, 2014] indicates that explicit treatment of heat and solute (salt) transfer by advection, groundwater hydrology, and buoyancy-driven flows is needed.

Using the central Canadian Beaufort Shelf as an example, we quantitatively investigate the role of submarine groundwater discharge on the temperature and salinity field and its effects on the seaward extent of relict submarine permafrost and gas hydrate stability on the circum-Arctic shelf under climate change. We show that a complex coupling exists between buoyancy- and pressure-driven flows, the salinity field, and permeability variations imposed by the evolving permafrost layer. Model results suggest that the role of heat and salt transport and its effect on permafrost evolution may provide context for the interpretation of recent methane flux field data in the Arctic.

2. Numerical Model Formulation

We model a two-dimensional sediment transect oriented perpendicular to the present-day shoreline located at the Canadian Beaufort Sea Shelf. The transect extends from the present-day shoreline to the shelf edge, $\sim 150 \text{ km}$ offshore [Blasco *et al.*, 2013], and to 1.5 km depth below the sediment surface. We use the numerical model to evaluate the evolution of temperature, pore water salinity, pressure, fluid velocity, permafrost distribution, and gas hydrate stability. The model is time dependent and based on the finite volume method previously documented in Frederick and Buffett [2014], with improvements and changes noted as follows. Because direct observations of the physical conditions at the Arctic are scarce, some

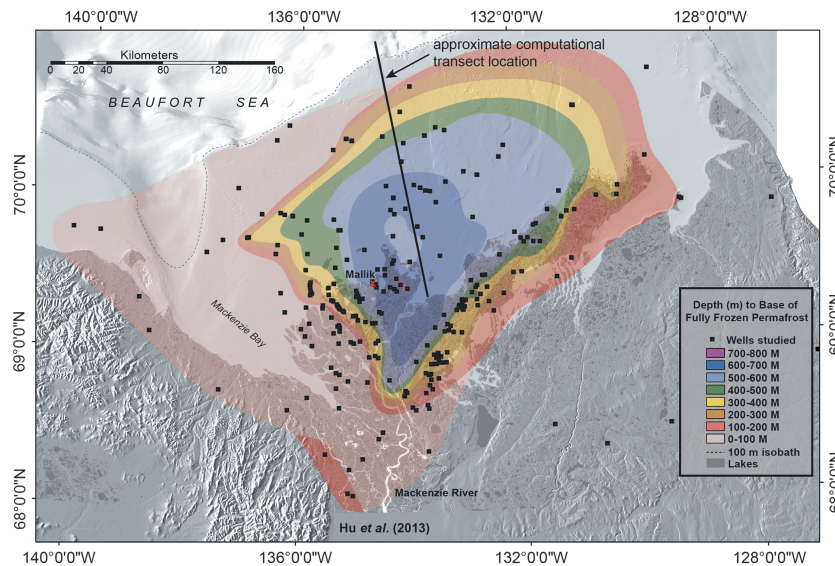


Figure 1. Map of the depth to the base of fully frozen, ice-bearing permafrost at the Canadian Beaufort Shelf, modified from *Hu et al. [2013]*. The approximate computational transect in this study is shown by the solid black line. Figure used with permission from the Natural Resources Canada under the Open Government License-Canada version 2.0.

approximation is necessary when choosing model parameters. A map of the study area and approximate location of the computational transect is shown in Figure 1.

The temperature field T is solved according to the energy equation,

$$\overline{\rho c_p} \left[\frac{\partial T}{\partial t} + \nabla \cdot (uT) \right] = \nabla \cdot (\mathbf{K} \cdot \nabla T) + \varphi_i \quad (1)$$

where ρ is the density, c_p is the specific heat, u is the transport velocity of the pore fluid, and φ_i is the latent heat of ice formation (for details on the treatment of latent heat and water/ice phase change, see *Frederick and Buffett [2014]*). The thermal conductivity is described by a tensor \mathbf{K} which imparts anisotropy. The density and specific heat within each computational grid cell are determined by a volume average of components (denoted by an overbar), while the components in the thermal conductivity tensor are obtained via a mixture model,

$$\mathbf{K} = K_{s_{xx}}^{(1-\phi)} K_f^{(S_f)} \mathbf{e}_x \mathbf{e}_x + K_{s_{yy}}^{(1-\phi)} K_f^{(S_f)} \mathbf{e}_y \mathbf{e}_y \quad (2)$$

which defines an effective value \mathbf{K} (expressed in dyadic notation) based on the volume fraction S of each component (e.g., rock ($S_s = 1 - \phi$), pore fluid ($S_f = \phi f$), or ice ($S_i = \phi i$)). We use the average background heat flow value of 54 mW m^{-2} as a (spatially and temporally constant) basal heat flux boundary condition, as measured near-shore at the U.S. Beaufort [*Deming et al., 1992*] and offshore at the Canadian Beaufort [*Judge and Majorowicz, 1992*]. A no-heat flux (insulating) boundary condition is applied at the two vertical sides.

To determine the gas hydrate stability zone, we determine the equilibrium temperature following the empirical relationship given by *de Roo et al. [1983]* using the local salinity and pressure. The salinity field \mathbb{C} is solved via the advection-diffusion equation,

$$\frac{\partial \mathbb{C}}{\partial t} + \nabla \cdot (u\mathbb{C}) = \mathbf{D} \nabla^2 \mathbb{C} + Q \quad (3)$$

where Q is a salt source term, which represents the influence of ice formation. \mathbf{D} is the effective diffusion coefficient for salt within marine sediments (details in *Frederick and Buffett [2013]*), given by

$$\mathbb{D} = \mathbb{D}_m \phi^{n-1} \quad (4)$$

which depends on the molecular diffusivity of salt in seawater, D_m . The exponent n is obtained empirically and depends on the depositional environment. The experiments of *King et al. [1988]* found values of n for Beaufort Sea permafrost sediments between $2 < n < 3$ for sands, $3 < n < 5$ for silts, and $5 < n < 8$ for clays.

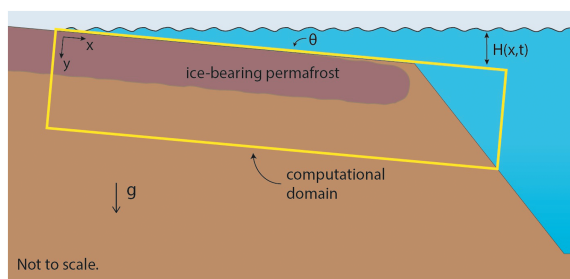


Figure 2. The yellow rectangle outlines the computational domain, which is aligned with the top of the shelf surface and tilted by a small angle θ . The schematic shows the system in a state of ocean transgression, with the origin located at the present-day shoreline. $H(x,t)$ is the water height above the domain and determines the top pressure boundary condition.

pore waters with salinity ranging from 4 to 11.5 ppt between 665 and 830 m depth, consistent with the regional studies. Details of the near-shore salinity are not as constrained at the Canadian Beaufort; however, records from the Mallik gas hydrate test well reported by Matsumoto *et al.* [2005] show that pore waters are fresh in the upper 1.1 km of sediment depth and then transition to ocean salinity values deeper. We use the near-shore salinity profile at Mallik as a boundary condition for the vertical boundary in the model located at the present-day shoreline. We use seawater values for the salinity boundary condition at depth.

Darcy's Law for fluid flux, or the transport velocity u , through a porous media with buoyancy [Andler and Brenner, 1988] is given by,

$$u = -\frac{\mathbf{k}(\phi)}{\mu} \nabla [P_{\text{total}} - (\rho g x \sin \theta) - (\rho g y \cos \theta)] \quad (5)$$

Here P is the total pressure, and μ is the fluid viscosity. Drill cores show the stratigraphy of the Canadian Beaufort Shelf is controlled by regressive/transgressive cycles which deposit alternating layers of fluvial sand or marine mud, respectively [Osterkamp, 2001]. This layering imparts an anisotropy to the sediment permeability tensor, $\mathbf{k}(\phi)$, where horizontal permeability is controlled by the sandy layers, and vertical permeability is limited by the marine mud/silt layers. Sediment layering is also thought to contribute to variations in the observed porosity at the Alaskan North Slope, where $22\% < \phi < 48\%$ [Collett *et al.*, 2011]. We set $k_{xx} = 1 \times 10^{-11} \text{ m}^2$, $k_{yy} = 1 \times 10^{-15} \text{ m}^2$, and $\phi = 0.35$, accordingly. While some of these observations are onshore, they are reasonable values to use given the uncertainties and the long terrestrial history over the last glacial cycle at the location of the computation transect.

The density of the pore fluid is calculated according to Fofonoff and Millard [1983] and accounts for pore fluid buoyancy as a result of salinity and temperature variations. Furthermore, we assume the permeability is function of porosity, based on a modified Kozeny-Carman relation [Mavko and Nur, 1997], and is coupled to changes in the permafrost. The computational domain is rotated by the angle θ so that the top of the domain aligns with the sediment surface of the shelf (see Figure 2 for a domain schematic). At both the Canadian and U.S. Beaufort, θ is much less than 1° (0.04° and 0.07° , respectively). We model a general case where the permeability tensor is not rotated with respect to the domain, meaning the sediment layers are parallel to the sediment (domain) surface and slope at the angle θ .

The hydrostatic pressure is applied as a boundary condition at the top of the domain, given by

$$P_h^{z=0} = \rho_f g H(x, t) \quad (6)$$

where $H(x, t)$ is the water depth as a function of the distance offshore and ρ_f takes the value for seawater. Hydrostatic pressure boundary conditions are applied at the base of the domain and at both sides. At the terrestrial side, the hydrostatic pressure applied includes a variable hydraulic head term which represents a variable water table height. The hydraulic head is updated in time to drive a constant specified flux of groundwater into the computational transect. At the Alaskan North Slope, Deming *et al.* [1992] estimated an average groundwater Darcy velocity based on deep heat flow variations of 70 mm yr^{-1} , corresponding to a

The strong dependence on sediment type produces strong anisotropy in sediments of alternating sand and silt/clay layers. In this study we assume that the diffusion coefficient is a tensor, where the horizontal diffusion coefficient is defined by n_{sand} , and the vertical diffusion coefficient is defined by n_{clay} .

Well log data at the Alaskan North Slope were used by Hanor *et al.* [2004] and Belanger [2007] to calculate the near-shore salinity with depth, which was relatively fresh between 0 and 10 ppt in the upper 1.25 km of sediment depth, with isolated, large seawater pockets deeper. At the Mount Elbert gas hydrate test well in Alaska, Torres *et al.* [2011] reported meteoric

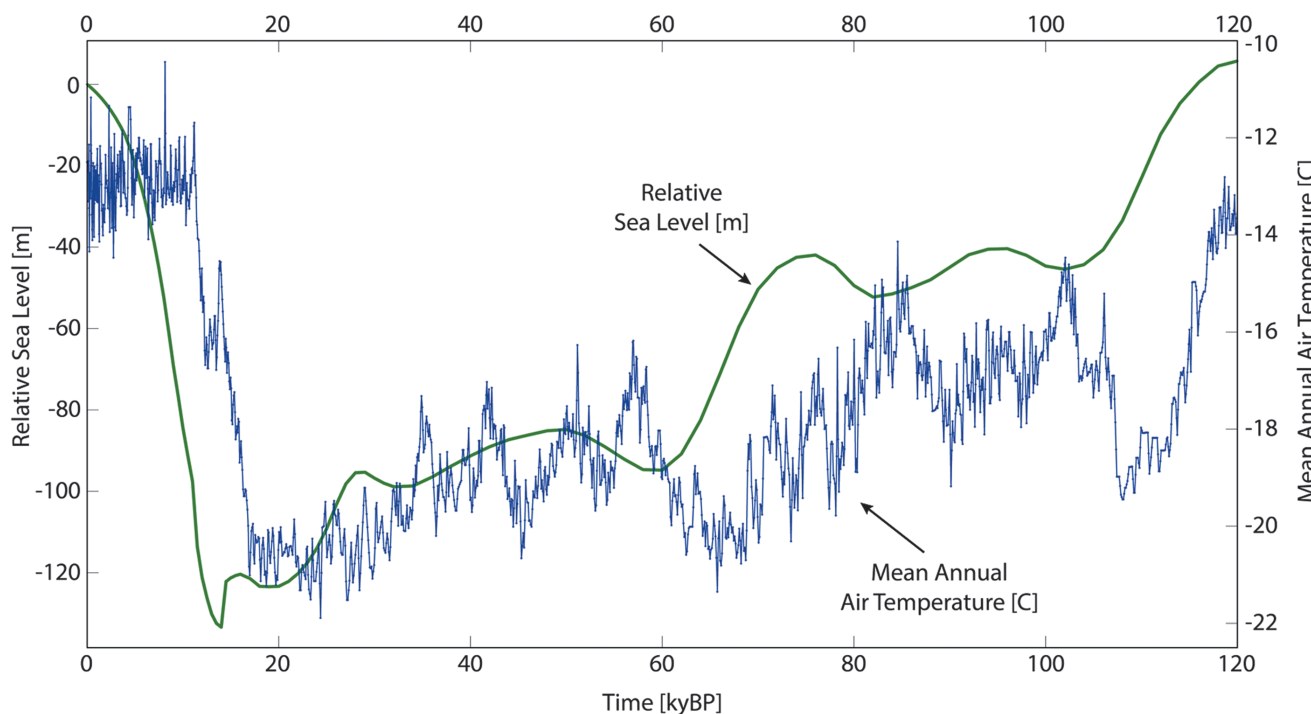


Figure 3. Relative sea level and mean annual air temperature at the Canadian Beaufort Sea Shelf for the last 120 ka [Peltier, 2004; Kendall et al., 2005; Petit et al., 1999]. When sediments are exposed subaerially, air temperature is applied as a boundary condition at the sediment surface. When sediments are submerged by the Arctic ocean, water depth and bottom water temperature determine the pressure and temperature boundary conditions at the sediment surface, respectively. For further details, see Frederick and Buffett [2014].

groundwater discharge flux of $140 \text{ m}^3 \text{ yr}^{-1} \text{ m}^{-1}$ of shoreline when integrated over the depth of the Deming et al. [1992] model. Similar patterns in heat flow variations were observed offshore at the Canadian Beaufort Shelf, but an estimate for groundwater discharge was not given [Judge and Majorowicz, 1992].

The timing of sediment exposure is determined by a site-specific sea level curve [Peltier, 2004; Kendall et al., 2005] spanning the last 120 ka. When sediments are exposed subaerially, air temperature records from the Vostok ice core deuterium data set [Petit et al., 1999, 2001], corrected to be site specific, are applied at the sediment surface. When sediments are submerged by the Arctic Ocean, water depth, ocean salinity, and bottom water temperature determine the pressure, salinity, and temperature boundary conditions at the sediment surface, respectively (see Figure 3 and full details in Frederick and Buffett [2014]). Ocean water temperature and salinity values as a function of depth are obtained from regional conductivity-temperature-depth casts archived in the *World Ocean Database* [2009]. Temperature and salinity data for an equal amount of summer and winter casts were averaged using Ocean Data View software [Schlitzer, 2014] to obtain representative mean annual values, which are used as the vertical boundary conditions on the right side of the domain and within the region of the domain that represents seawater. Ocean bottom water temperatures are typically below 0°C in the near-shore Arctic Ocean. For example, mean annual calculated ocean water temperature ranges between -0.39°C and -1.46°C in the upper 140 m water column.

Fluid volume fraction S_f is updated in time by

$$\frac{\partial S_f}{\partial t} + \nabla \cdot u = \Phi_f \quad (7)$$

where Φ_f represents a source/sink of fluid when ice melts/forms, respectively. The fluid source term is given by

$$\Phi_f = - \left(\frac{\rho_i}{\rho_f} \right) \frac{\partial S_i}{\partial t} \quad (8)$$

but we assume $\rho_i/\rho_f \approx 1$, which neglects the small volume change when water changes phase to/from ice.

Table 1. All Model Parameters Used Are Listed in the Table Below and Are Assumed Constant^a

Symbol	Parameter	Value	Units	Reference
C_w	seawater salinity b.c.	24–35	ppt	WOD [2009]
ϕ	sediment porosity	0.35		Collett <i>et al.</i> [2011]
ϕ_0	percolation porosity ^b	0.01		
k_{xx}	horizontal sediment permeability ^c	1×10^{11}	m^2	
k_{yy}	vertical sediment permeability ^d	1×10^{15}	m^2	
μ_f	pore water viscosity	1.8×10^{-3}	Pa s	Lide [2013–2014]
ρ_f	density of fresh pore water	1000	$kg\ m^3$	Lide [2013–2014]
ρ_i	density of ice	920	$kg\ m^3$	Lide [2013–2014]
ρ_s	density of sediments ^b	2700	$kg\ m^3$	
$\frac{\partial T}{\partial z}$	geothermal gradient b.c.	26.5	$C\ km^{-1}$	Weaver and Stuart [1983]
Cp_f	heat capacity of pore water	4.18	$kJ\ kg^{-1}\ C^{-1}$	Lide [2013–2014]
Cp_i	heat capacity of ice	2.09	$kJ\ kg^{-1}\ C^{-1}$	Lide [2013–2014]
Cp_s	heat capacity of sediments ^b	0.92	$kJ\ kg^{-1}\ C^{-1}$	
L_f	latent heat of pore water	334	$kJ\ kg^{-1}$	Lide [2013–2014]
K_f	thermal conductivity of pore water	0.58	$W\ C^{-1}\ m^{-1}$	Lide [2013–2014]
K_i	thermal conductivity of ice ^e	4.0	$W\ C^{-1}\ m^{-1}$	
K_{sxx}	horizontal thermal conductivity of sediments ^f	5.0	$W\ C^{-1}\ m^{-1}$	
K_{syg}	vertical thermal conductivity of sediments ^g	4.0	$W\ C^{-1}\ m^{-1}$	

^aThe references listed provided guidance in our choice of parameter values; b.c. refers to boundary condition.^bTypical values used for marine sediments.^cPermeability value is typical for coarse sand (quartz).^dPermeability value is typical for mud/silt.^eThis value was chosen to match observed permafrost depth and temperature profiles.^fBulk thermal conductivity is $2.35\ W\ C^{-1}\ m^{-1}$ given $\phi = 0.35$ pore volume saturated with water.^gBulk thermal conductivity is $2.03\ W\ C^{-1}\ m^{-1}$ given $\phi = 0.35$ pore volume saturated with water.Pressure P is computed from conservation of mass

$$\nabla \cdot u = 0 \quad (9)$$

The coupled equations are solved iteratively using a preconditioned general minimum residual method at each time step. The model is run for several successive glacial cycles for each value of groundwater discharge chosen until a quasi-steady salinity field and permafrost distribution is established. We begin all simulations with no existing permafrost and explore the results for initial conditions of fresh pore water salinity and a temperature field set to the geothermal gradient in equilibrium with the coldest glacial mean annual air temperature. For comparison, we also run the model with initial conditions of ocean pore water salinity, a temperature field set to the geothermal gradient in equilibrium with the ocean bottom water temperature, and no submarine groundwater discharge. The results presented begin at the sea level low (18 kaBP) and extend to the present-day time. No potential anthropogenic effects are included in the simulations. All model parameters are listed in Table 1.

3. Observations of Ice-Bearing Submarine Permafrost

Several methods have been used to make observations of the submarine permafrost distribution on the Arctic continental shelf. While drilling can give us direct observations, information is limited to near the drill site only. On the other hand, geophysical observations such as seismic or electromagnetic ship surveys can inform us about the sediments over wide regions, but the data are indirect and must be carefully interpreted to give meaning. Using multiple data sets obtained with a variety of methods should give the most accurate picture. This integrated approach was used by Hu *et al.* [2013] to create a map of the ice-bearing permafrost depth at the Canadian Beaufort Shelf (see Figure 1), using conventional well logs and well seismic and temperature survey data. Hu *et al.* [2013] found that permafrost extends deepest near

Richardson Island (720 m below seafloor (bsf)) and gradually decreases in depth north, toward the shelf edge, and to the east. Permafrost thins rapidly west, toward the Mackenzie Trough region, and is most likely absent in the modern Mackenzie Delta due to heat input from the Mackenzie River. At the U.S. Beaufort, less information is available to constrain submarine permafrost extent. *Brothers et al.* [2012] analyzed prestack multichannel seismic data using a seismic-refraction-velocity-based method to map ice-bearing sediment and found that permafrost extends seaward out to 20 m water depth, or approximately 30 km offshore.

When comparing model results to seismic observations of permafrost distribution, it is important to understand the differences than can arise simply due to the method of observation. Theory can give insight when interpreting seismic velocity of partially to fully ice-bearing marine sediments. *Johansen et al.* [2003] determined the seismic p wave velocity as a function of ice saturation in the pore space of granular materials with a hybrid theoretical approach. Under this theory, little velocity perturbation (0–6%) is expected for sediments with ice occupying < 40% of the pore space for porosity between $0.36 < \phi < 0.38$. However, ice occupying > 40% pore space shows a significant step increase in the velocity perturbation of the presented granular materials, by 32 to 65%, relative to the unfrozen value [*Johansen et al.*, 2003]. This behavior implies that partially frozen sediments (< 40%) may be undetected by seismic-refraction-velocity-based methods, and arguably impossible to map, due to the negligible velocity perturbation. For example, in the Mackenzie Delta area of the Canadian Beaufort Shelf, p wave velocity through unfrozen sediment ranged between 1524 and 1981 m s⁻¹, while for sediments interpreted as frozen, p wave velocity ranged between 2438 and 4267 m s⁻¹ [*Hatlelid and MacDonald*, 1982], an average velocity increase of 41%. At the U.S. Beaufort, *Brothers et al.* [2012] measured the p wave velocity of unfrozen sediments between 1700 and 2100 m s⁻¹, while velocities ≥ 2300 m s⁻¹ were interpreted as frozen sediments. Results from laboratory studies on sediment samples from the Beaufort Sea and near the Mackenzie River by *King et al.* [1982] indicate unfrozen sediment p wave velocity ranged between 1500 and 1658 m s⁻¹, while frozen sediments (as determined by temperature, not ice content) had widely ranging values between 1570 and 4250 m s⁻¹. The large range in frozen sediment p wave velocity of the experiments is likely due to variations in sediment material, salinity, and ice saturation in the pore space. For example, a frozen clay sample had the same p wave velocity as an *unfrozen* sand sample in the experiments [*King et al.*, 1982]. Therefore, observations of permafrost using seismic velocity are likely capturing ice-bearing sediments occupying more than 40% of the pore space and thus represent a conservative mapping.

Electrical resistivity is another common technique used in detecting ice-bearing sediments but tends to be conservative for similar reasons as seismic velocity interpretations. *King et al.* [1988] measured the electrical resistivity of several Beaufort Sea permafrost samples and formed a relationship between the resistivity ratio of the sediments and the pore water fraction. The result is a highly nonlinear behavior, where resistance relative to unfrozen sediments increases exponentially as ice occupies more of the pore space, given by

$$R_f/R = f^{1-n} \quad (10)$$

where R_f/R is resistivity ratio of frozen relative to unfrozen material, f is the fluid saturation in the pore space, and n is the empirically determined Archie constant [*King et al.*, 1988]. When ice occupies only a small amount of the pore space (i.e., when f is close to unity), there is little increase in the resistivity predicted, making it difficult to observe frozen sediments occupying low pore volumes with certainty. For example, well logs presented by *Weaver and Stuart* [1983] were interpreted as ice bearing (or hydrate bearing) when resistivity increased by a factor of 100 relative to the unfrozen sediments. Given the sediments are sand dominated (e.g., $n = 3$ [*King et al.*, 1988]), the electrical resistivity method is detecting frozen sediments where water occupies less than 10% pore volume, or equivalently, ice occupies more than 90% of the pore space. Allowing for a mix of sand and clay (e.g., $n = 6$ [*King et al.*, 1988]), the electrical resistivity method is detecting frozen sediments where water occupies less than 40% pore volume, or equivalently, ice occupies more than 60% of the pore space. Like the seismic velocity method, using changes in the electrical resistivity to detect ice also represents a conservative mapping.

To provide a more accurate comparison between model results and field observations, we provide additional interpretation of the model results according to the expected p wave velocity perturbation and resistivity ratio relative to unfrozen sediments, following the studies by *Johansen et al.* [2003] and *King et al.* [1988], respectively. Moreover, we define “detectable” permafrost as frozen sediments with ice occupying > 40% pore volume (assuming 0.35 porosity).

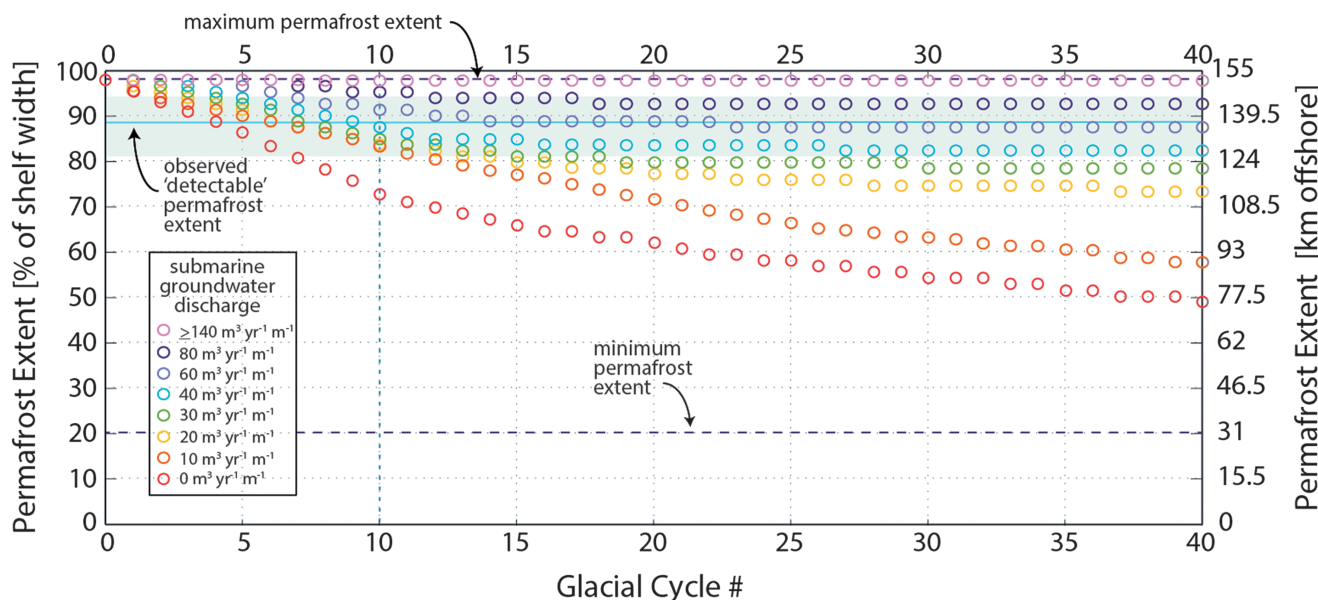


Figure 4. Colored open circles indicate the modeled permafrost extent offshore at the present-day equivalent time over 40,100 ka equivalent glacial cycles for several values of submarine groundwater discharge rate at the Canadian Beaufort Shelf computational transect. Permafrost extent shows transient behavior over potentially long time scales, making it difficult, if not impossible, to predict the present rate of groundwater discharge based on observed permafrost extent. A discharge rate of $60 \text{ m}^3 \text{ yr}^{-1} \text{ m}^{-1}$ provides the best match between observed permafrost extent and the modeled, quasi-steady permafrost extent. The tenth glacial cycle is marked for reference (see text for explanation).

4. Model Results

4.1. Offshore Freshening Via Submarine Groundwater Discharge

The salinity of the pore water is an important control on water phase change and therefore has a large effect on the evolution of relict submarine permafrost in the model. Because the offshore extent of relict submarine permafrost evolves over each glacial cycle, the resulting feedback between the permeability variations imposed by the permafrost layer and pore water freshening from groundwater discharge introduces significant complexity. As a consequence of this coupling, the location of the brackish mixing zone displays transient behavior that lasts several glacial cycles in duration and depends on the strength of the groundwater discharge.

Results presented in Figure 4 are obtained by running the numerical model over several successive and equivalent 100 ka glacial cycles at the Canadian Beaufort Shelf, allowing the fluid-confining permafrost layer to evolve under periodic forcing. The seaward extent of the detectable submarine permafrost layer (in percent of the shelf width and kilometers offshore) is recorded at the present-day equivalent point in time at each glacial cycle and for each value of submarine groundwater discharge tested. In all but the largest value of submarine groundwater discharge tested, the initial transient behavior in the evolution of submarine permafrost extent lasts longer than one glacial cycle. Interestingly, the permafrost extent is still evolving for some values of submarine groundwater discharge after 40 equivalent 100 ka glacial cycles. One hundred thousand year glacial cycling in the Arctic has only occurred over the past 1 Ma [Lisicki and Raymo, 2005]; thus, only about ten,100 ka glacial cycles could have occurred within this time. The tenth glacial cycle is marked in Figure 4 as a point of reference and is not intended to imply any physical meaning. We note that this approach neglects the shorter, 41 ka period cycles.

The seaward extent of the permafrost at the present-day equivalent for each value of groundwater discharge is bounded by minimum and maximum values. The minimum permafrost extent is determined by running the model without groundwater discharge and with sediments of ocean water salinity. In this case, because the sediments are entirely saline, the ice melting point is the lowest (e.g., -1.8°C for 32 ppt salinity), and the least amount of ice remains by the present day. On the other hand, the maximum permafrost extent is determined by running the model with entirely fresh sediments; thus, the melting point for ice is the highest (e.g., 0°C). Additionally, because mean annual ocean bottom water temperatures are below 0°C ,

the maximum permafrost extent in this case is controlled by the position of the lowest sea level, which determines the maximum shelf exposure (e.g., 140 m sea level drop or 153 km offshore at the Canadian Beaufort, and 84 km offshore at the U.S. Beaufort).

Because the initial conditions chosen for all simulations in Figure 4 represent terrestrial conditions (i.e., a state of ocean regression), the detectable permafrost extent begins at the maximum value for glacial cycle 0. In subsequent cycles, the offshore extent of the permafrost at the present-day equivalent time decreases with each glacial cycle until a steady state permafrost extent is reached. This behavior is due to shelf sediment “salinization” as a result of buoyancy-driven flow and the lower melting temperature for ice in saline pore water. Because salty water is denser than fresh water, salty pore fluids from far offshore tend to flow inland and downward, shrinking or displacing the freshwater aquifer with each glacial cycle. However, if a sufficient freshwater head is present near the shore, saltwater migration inland is opposed by an offshore flow of freshwater. The permafrost extent offshore becomes quasi-steady when the salinity field reaches an equilibrium. This occurs when a balance of density and pressure-driven flows is established with the permeability variations imposed by the overlying permafrost layer, and the saltwater-freshwater transition location becomes quasi-stationary. Results suggest that as the strength of the groundwater discharge increases, the equilibrium offshore permafrost extent also increases (e.g., moves seaward).

The offshore permafrost extent can display transient behavior over potentially long time scales because density-driven groundwater flow is slow (typically $0.01\text{--}1 \text{ m yr}^{-1}$) and the continental shelf is very large (typically 150 km at the Canadian Beaufort and several times larger at the East Siberian Arctic Shelf).

Moreover, permeability variations imposed by the overlying permafrost layer restrict vertical flow during most of the glacial cycle, preventing saltwater from entering shelf sediments from above. The number of glacial cycles required to reach a quasi-steady permafrost extent appears to depend on how “far” the initial or current conditions are from the equilibrium conditions. Thus, we note that the trends shown in Figure 4, in terms of the number of glacial cycles required to reach equilibrium, reflect the particular choice of initial conditions in the simulations (e.g., a state of ocean regression). For example, simulations with larger values of groundwater discharge reach a quasi-steady permafrost extent in fewer glacial cycles than simulations with lower values because salinization is resisted, thus maintaining a condition more similar to the chosen initial state of ocean regression. The results in Figure 4 suggest that groundwater discharge rates of $\geq 140 \text{ m}^3 \text{ yr}^{-1} \text{ m}^{-1}$ are strong enough to prevent salinization of the shelf sediments where the permafrost layer forms. On the other hand, the case where groundwater discharge is absent allows for the most rapid salinization rate; however, since the permafrost responds very slowly, permafrost extent offshore continues to evolve even after 40 glacial cycles (a time much longer than the Arctic has been experiencing 100 ka glacial cycling).

The transient behavior displayed in Figure 4 makes it difficult, if not impossible, to estimate the present rate of submarine groundwater discharge based on the detectable permafrost extent offshore. While the value of groundwater discharge for the Beaufort Shelf via onshore heat flow variations was estimated at $140 \text{ m}^3 \text{ yr}^{-1} \text{ m}^{-1}$, in order to match the modeled to the observed permafrost extent after a quasi steady state is reached, a groundwater discharge of $60 \text{ m}^3 \text{ yr}^{-1} \text{ m}^{-1}$ is required. However, this does not imply that $140 \text{ m}^3 \text{ yr}^{-1} \text{ m}^{-1}$ is an incorrect estimate of groundwater discharge for the present day. Rather, it is possible that the permafrost on the Canadian Beaufort Shelf is still responding to a lower value of groundwater discharge that existed in the past. The effects of transient, unsteady groundwater discharge is a future direction of research.

While the long response times and the nonlinear coupling between the density-driven fluid flow and variations imposed on the permeability due to the permafrost layer are complex, the results in Figure 4 have some clear implications. The minimum permafrost extent offshore predicted by the model at the Canadian Beaufort Shelf suggests that even if the shelf originated as terrestrial, the observed permafrost is difficult to explain without some resistance to salinization of the pore fluids. We hypothesize that the resistance to salinization is most likely due to groundwater discharge in the shelf sediments, but alternatively, salinization may be slower than predicted in the model if sediment permeability is reduced or local sea level was significantly lower in the past glacial cycles than the most recent glacial cycle. Moreover, variations in the submarine groundwater discharge clearly result in potentially large differences in the detectable permafrost extent offshore. These results imply that the local hydrology may be as large of a factor as sea level history or paleoclimatic conditions in controlling the present-day extent of relict submarine permafrost.

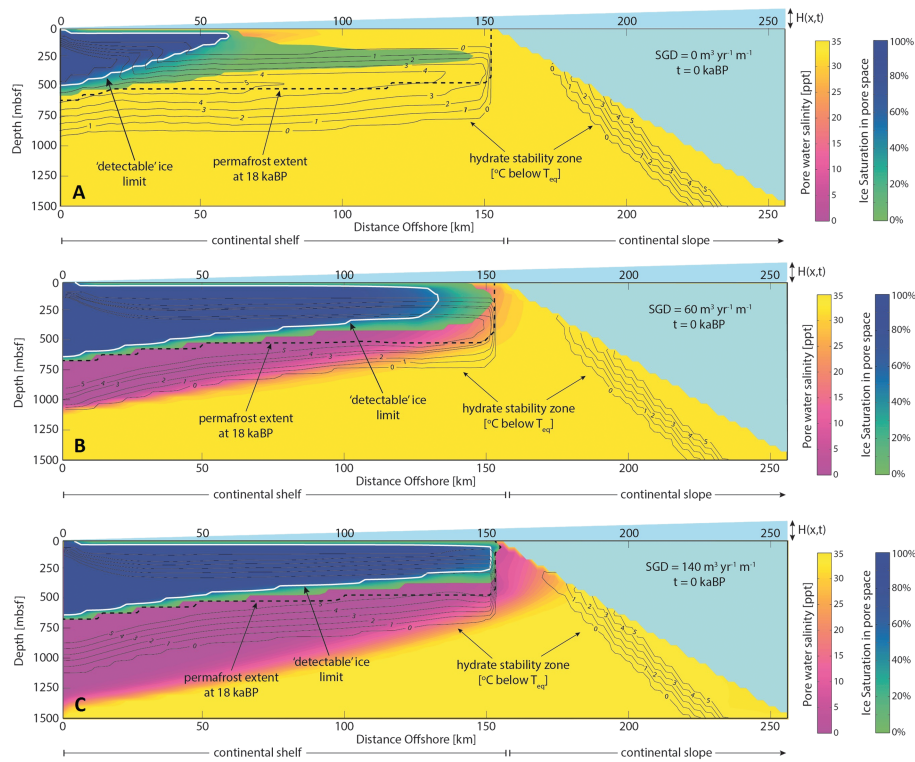


Figure 5. Modeled permafrost, salinity, and gas hydrate stability at the present-day time at the Canadian Beaufort transect for (a) $0 \text{ m}^3 \text{ yr}^{-1} \text{ m}^{-1}$, (b) $60 \text{ m}^3 \text{ yr}^{-1} \text{ m}^{-1}$, and (c) $140 \text{ m}^3 \text{ yr}^{-1} \text{ m}^{-1}$ groundwater discharge rates. The detectable permafrost limit is indicated by the solid white boundary. Hydrate stability is shown in terms of $^{\circ}\text{C}$ below hydrate melting temperature, or T_{eq} . Permafrost and a zone of hydrate stability remain in all three cases but are the least decayed when the shelf sediments contain a freshwater aquifer (Figures 5b and 5c) and the most decayed when the sediments are saline (Figure 5a). Quasi-steady results are shown.

4.2. Permafrost and Gas Hydrate Stability

Gas hydrate stability and the permeability of the shelf sediments to gas migration is closely linked with relict submarine permafrost. Moreover, gas hydrate stability is also affected by the salinity of the pore water; thus, differences in the submarine groundwater discharge also cause variations in the gas hydrate stability zone on the continental shelf and slope. Figures 5 and 6 show the model results for the permafrost distribution, salinity field, and hydrate stability zone (in terms of the sediment temperature below methane hydrate's melting point, or T_{eq}) within the two-dimensional transect after a quasi steady state has been reached in the permafrost extent for 0, 60, and $140 \text{ m}^3 \text{ yr}^{-1} \text{ m}^{-1}$ groundwater discharge rates at the present day and Last Glacial Maximum. The large freshwater aquifer which is maintained by groundwater discharge can clearly be seen in Figures 5b, 5c, 6b, and 6c. In contrast, when submarine groundwater discharge is absent (Figures 5a and 6a), the majority of the shelf sediments have become saline, and the freshwater aquifer only remains present within the frozen permafrost layer. Because the frozen sediments are highly impermeable, salinization into the permafrost layer is slow, which explains the long response times seen in Figure 4.

Figure 5 shows the two-dimensional transect at the present day (a state of ocean transgression). In all three cases of submarine groundwater discharge shown, the permafrost layer and hydrate stability zone remain, but they exist in various states of decay. The permafrost layer and hydrate stability zone are the least decayed when the shelf sediments contain a freshwater aquifer (Figures 5b and 5c) and the most decayed when the sediments are saline (Figure 5a). Relative to the last glacial maximum (Figure 6), ocean transgression causes the detectable permafrost zone (indicated by the solid white outline) to move inland and thin out. However, highly degraded, low-ice saturation permafrost still exists all the way out to the shelf edge in all three cases. Although undetectable by common geophysical methods, this actively degrading permafrost allows the hydrate stability zone to persist on the shelf at the present day because warming

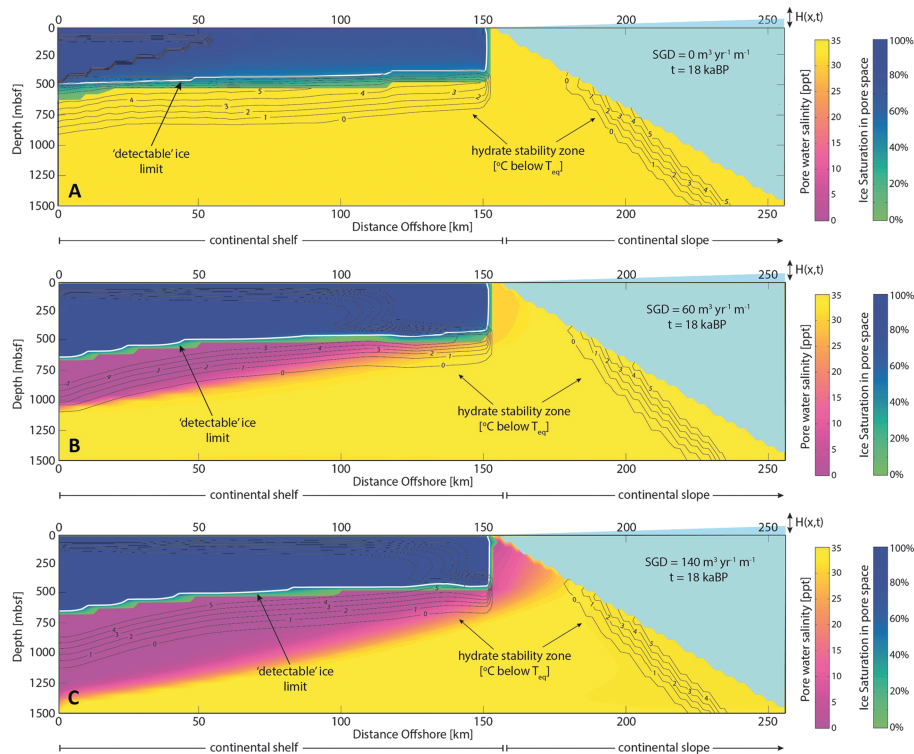


Figure 6. Modeled permafrost, salinity, and gas hydrate stability at the last glacial maximum at the Canadian Beaufort transect for (a) $0 \text{ m}^3 \text{ yr}^{-1} \text{ m}^{-1}$, (b) $60 \text{ m}^3 \text{ yr}^{-1} \text{ m}^{-1}$, and (c) $140 \text{ m}^3 \text{ yr}^{-1} \text{ m}^{-1}$ groundwater discharge rates. The detectable permafrost limit is indicated by the solid white boundary. Hydrate stability is shown in terms of $^{\circ}\text{C}$ below hydrate melting temperature, or T_{eq} . At this time (a state of ocean regression), the permafrost is terrestrial and forms a thick layer even within saline groundwater as shown in Figure 6a. Quasi-steady results are shown.

from above is buffered by the permafrost layer's latent heat sink. As a result, very little change in the hydrate stability zone on the shelf is predicted, except near the shelf edge where the degree of stability is reduced but not entirely eliminated.

Figure 7 shows the temperature field and Darcy velocity field within the two-dimensional transects at the present day for the same cases presented in Figure 5. The detectable permafrost and boundary representing the extent of freshening in Figure 5 is also included for reference. In all cases, shelf sediments are still much cooler than slope sediments today because the presence of the permafrost layer, with its large latent heat sink, slows warming of the shelf after submergence. As a result, a large kink in the temperature field exists at the shelf break. When groundwater discharge is present (Figures 7b and 7c), fresh terrestrial pore fluid flows beneath the permafrost layer toward the shelf edge. Once the flow reaches the seaward permafrost boundary, it discharges to the sediment surface, forming a submarine freshwater spring. The rate of groundwater discharge controls the depth and thickness of the offshore flow. Without the dominant offshore flow, only geothermally driven circulation (which is much smaller in magnitude) can be seen in Figure 7a.

Submarine groundwater discharge modifies the temperature field through the advection of heat. Figure 8 shows the temperature perturbation caused by (a) 60 and (b) $140 \text{ m}^3 \text{ yr}^{-1} \text{ m}^{-1}$ groundwater discharge rates relative to no discharge (e.g., $0 \text{ m}^3 \text{ yr}^{-1} \text{ m}^{-1}$). Figure 8 indicates that submarine groundwater discharge results in warming beneath the permafrost layer on the midshelf, and the warming influence extends farther offshore as the strength of the groundwater discharge increases. Midshelf warming is due to the vertical component of the submarine groundwater flow field, which enhances vertical heat transport by advection in comparison to the temperature field when groundwater discharge is absent. Midshelf warming is also responsible for the thinner gas hydrate stability zone in Figures 5b and 5c relative to Figure 5a. Moreover, an abrupt, thin vertical zone of cooling is predicted at the shelf edge, as groundwater discharge carries cooler water below the permafrost layer toward the warmer sediments in the slope. The cooling effect at the shelf

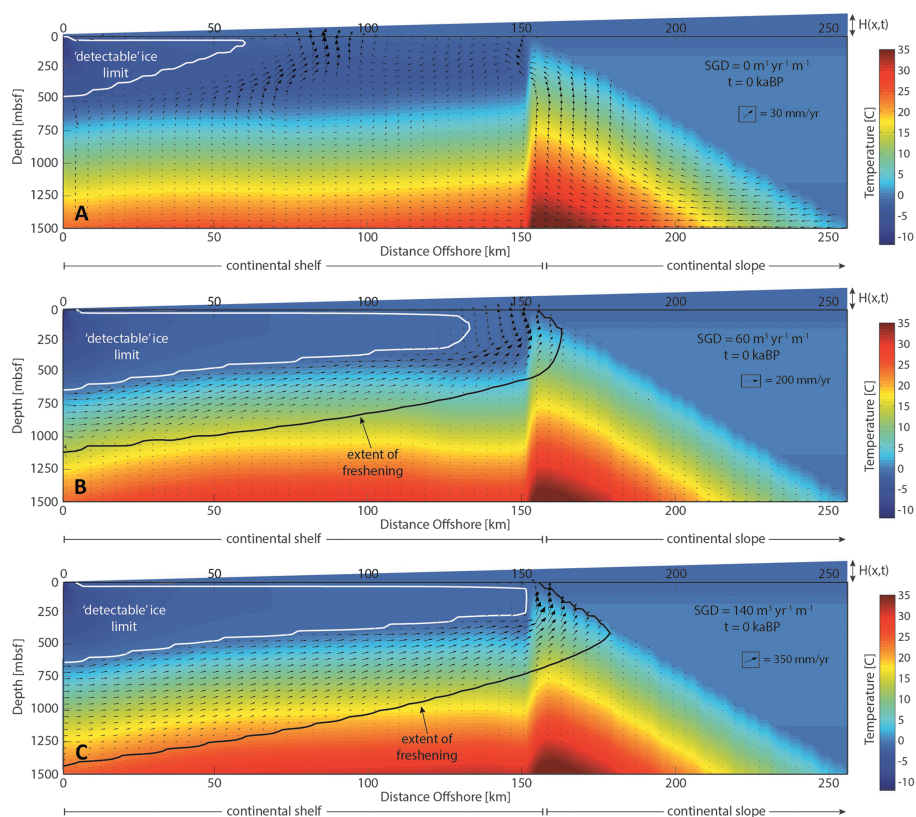


Figure 7. Modeled temperature field and Darcy velocity within the marine sediments at the present-day time at the Canadian Beaufort transect for (a) $0 \text{ m}^3 \text{ yr}^{-1} \text{ m}^{-1}$, (b) $60 \text{ m}^3 \text{ yr}^{-1} \text{ m}^{-1}$, and (c) $140 \text{ m}^3 \text{ yr}^{-1} \text{ m}^{-1}$ groundwater discharge rates. Detectable permafrost is indicated by the solid white boundary, while the extent of pore water freshening is indicated by the solid black boundary. When no groundwater discharge exists as shown in Figure 7a, pore fluid circulates as driven by geothermally induced buoyancy forces. On the other hand, submarine groundwater discharge flows offshore as shown in Figures 7b and 7c and has an upward component, carrying heat but also fresh pore fluid. Quasi-steady results are shown.

edge can also be seen as a reduction in the steepness of the temperature kink (Figure 7) as the strength of the discharge increases. However, the thermal influence of submarine groundwater discharge appears to weaken substantially beyond the shelf break.

Gas hydrate stability on the continental slope is not significantly affected by the rates of submarine groundwater discharge studied, except for the largest rate (e.g., $140 \text{ m}^3 \text{ yr}^{-1} \text{ m}^{-1}$) tested. As shown in Figure 5c, the hydrate stability zone extends to a higher elevation on the upper slope when submarine groundwater discharge is strong. The increase in stability is due to the pore fluid freshening, and not a temperature influence (see Figure 8b). Additionally, because ocean bottom water temperatures were held constant on the continental slope, the increase in hydrostatic pressure due to ocean transgression actually increases the zone of hydrate stability on the continental slope compared to the Last Glacial Maximum.

5. Discussion

The size of the freshwater aquifer on the circum-Arctic continental shelf is unknown, but many indirect observations hint at its presence. Geochemical analysis at the Mallik gas hydrate test well indicates that the pore water is fresh to brackish in the upper 1100 m of sediment depth, with pore water salinity increasing to seawater values deeper [Matsumoto *et al.*, 2005]. Moreover, high saturation hydrate was found in intervals between 890 and 1108 m bsf. These observations are consistent with the model predictions for an intermediate groundwater discharge rate (Figure 5b), where the freshwater aquifer and hydrate stability zone extends to roughly 1100 m depth at the present-day shoreline. While Matsumoto *et al.* [2005] suggest that the relatively fresh pore water within the hydrate intervals may be due to local gas hydrate dissociation, our model suggests that submarine groundwater discharge provides an alternative scenario. Without some

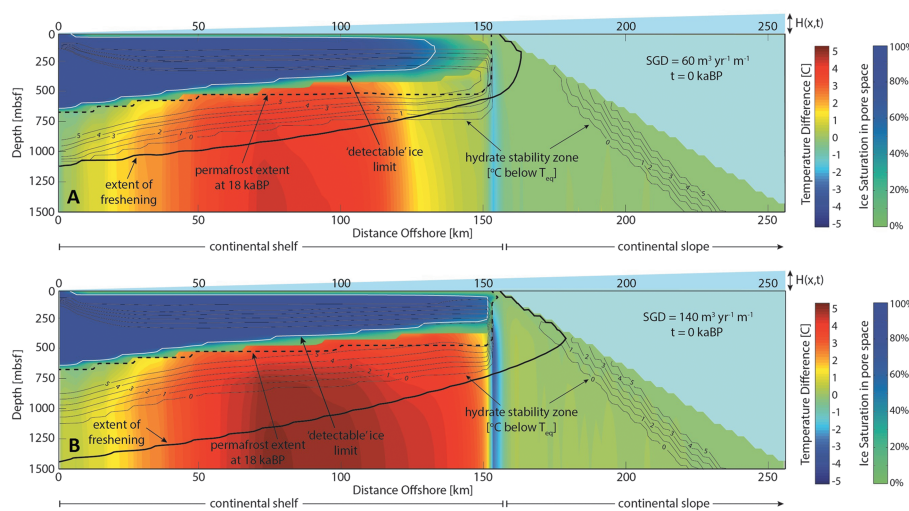


Figure 8. Modeled temperature field difference between (a) $60 \text{ m}^3 \text{ yr}^{-1} \text{ m}^{-1}$ and no groundwater discharge (e.g., $0 \text{ m}^3 \text{ yr}^{-1} \text{ m}^{-1}$) and (b) $140 \text{ m}^3 \text{ yr}^{-1} \text{ m}^{-1}$ groundwater discharge rates and no groundwater discharge at the present-day time at the Canadian Beaufort transect. Detectable permafrost at the present day is indicated by the solid white boundary, permafrost extent at the Last Glacial Maximum is indicated by the dashed black boundary, and the extent of pore fluid freshening is indicated by the solid black boundary. Groundwater discharge causes significant warming below the permafrost layer on the midshelf relative to no groundwater discharge. Warming of $\ll 1^\circ\text{C}$ is also predicted on parts of the slope.

preexisting and external source of freshening, our model shows that gas hydrate deposits should not be stable within the intervals found at the Mallik test well (compare Figure 6a and Figures 6b and 6c between 890 and 1108 m bsf).

Isotopic and major ion chemistry recently reported by *Gwiazda et al. [2014]* from piston and gravity cores at the Beaufort Shelf indicate downcore mixing between seawater and a freshwater end-member with a Mackenzie River-like composition. The background shelf and slope show influence of freshwater similar to the present meteoric water, while fluids escaping from pingo-like features on the midshelf have isotopic characteristics that may suggest meteoric water that precipitated under different climatic conditions from the present. While it is unknown if the sediments of the Canadian Beaufort Shelf were originally fresh, the composition of the pore fluids reported by *Gwiazda et al. [2014]* are consistent with submarine groundwater discharge that is heavily influenced by the Mackenzie River hydrologic system, or that originated as recharge from precipitation during a past, different climatic condition. Moreover, our numerical model predicts that the midshelf is a region of upwelling and warming when submarine groundwater discharge exists. Therefore, submarine groundwater discharge may aid the formation of pingo-like features (as described by *Paull et al. [2007]*) on the Canadian Beaufort midshelf by providing a source of warming from below that is in addition to the geothermal heat flux.

This study finds that submarine groundwater discharge may play a large role in submarine permafrost evolution and gas hydrate stability and suggests that local hydrology may control the evolution of submarine permafrost as strongly as sea level variations, or paleoclimatic, for example. Additionally, when paleoclimatic history is similar between two regions, differences in local hydrology may explain large differences in submarine permafrost distribution. For example, detectable submarine permafrost exists on the majority of the Canadian Beaufort Shelf (up to 100 m water depth) [*Hu et al., 2013*], but only to 20 m water depth at the Alaskan Beaufort [*Brothers et al., 2012*]. While the geologic and sedimentation histories are different, the two locations have most likely experienced a similar paleoclimate to the extent that the model can resolve. If surface discharge is proportional to groundwater flow, then one interpretation for the difference in submarine permafrost extent is that Canada's Mackenzie River basin is more hydrologically active than the Alaskan North slope. To match the permafrost observations at the Canadian Beaufort, the model requires a submarine groundwater discharge of $60 \text{ m}^3 \text{ yr}^{-1} \text{ m}^{-1}$. On the other hand, to match the permafrost observations at the Alaskan Beaufort, a smaller groundwater discharge of $15 \text{ m}^3 \text{ yr}^{-1} \text{ m}^{-1}$ is required. Alternatively, differences in the lithology (sediment type, porosity, or faulting) which strongly

influence ice formation, cause more rapid salinization, or bias submarine permafrost detection, are other interpretations for the observed differences.

Model results imply that gas hydrate stability on the Beaufort Shelf may be more widespread than currently thought because the amount of permafrost we can detect by common geophysical methods is conservative. We have defined detectable permafrost (for purposes in this study) as ice-bearing sediments where ice occupies > 40% of the pore space (see section 3). However, as shown in Figure 5, a substantial amount of highly degraded, low-ice saturation permafrost still exists seaward of the detectable limit, allowing gas hydrate stability seaward of the detectable permafrost boundary. This result is consistent with findings reported by *Pohlman et al. [2012]* and *Ruppel et al. [2013]*, who did not detect systematic changes in seawater methane concentrations when crossing from near-shore sediments underlain by seismically detected permafrost to sediments lacking such permafrost on the Alaskan Beaufort Shelf.

Submarine groundwater discharges, as simply modeled in this study, does not seem to affect continental slope hydrates unless discharge rates are very strong. This is consistent with the recent modeling study by *Phrampus et al. [2014]*, which found submarine groundwater discharge an unlikely scenario to explain the discrepancy between observed and predicted bottom simulating reflectors, because sufficient cooling by offshore groundwater flow required an unrealistically thick plume, or a thinner but faster plume with velocity 5 or more times faster than estimated by *Deming et al. [1992]*. However, observations of submarine freshwater springs on the Beaufort Shelf slope do exist and may reflect concentrated flow of submarine groundwater through a more complex lithology. For example, *Pohlman et al. [2011]* described meteoric fluids originating from a Tertiary-aged continental aquifer discharging from a gas hydrate-bearing seep, called the Canning Seafloor Mound, located roughly 150 km offshore of the North Slope Alaska at water depth of about 2500 m on the Beaufort Sea continental slope.

While the model developed in this study is complex, limitations do exist. We have considered two-dimensional flow, but flows in all three dimensions no doubt occur on the shelf. Because of resolution limits and a desire for broad model applicability, we did not model local distinct lithologic units, such as alternating layers or blocks of sand, clay, shale, or limestones. Instead, we captured sediment layering with sediment anisotropy in permeability and thermal conductivity, with parameter values chosen that are typical of the lithologies found on the Beaufort shelf. However, variations in permeability due to local lithology, or a rotation in the permeability tensor due to sloping bedding layers, will effect fluid velocity, mass transport, and the time required for the salinity field and permafrost extent to reach a quasi steady state. Additionally, some model runs with larger vertical permeability (i.e., $1 \times 10^{-12} \text{ m}^2$, typical for coarse sand or fractured zones) revealed convective instabilities and salt fingering, increasing the effectiveness of salinization (similar to studies by *Kooi and Groen [2000]*, *Post and Kooi [2003]*, and *Cohen et al. [2010]*) and permafrost inhomogeneity on the shelf. Unfrozen, high-salinity intervals have been reported within the permafrost at the Alaskan North Slope, for example [*Collett and Bird, 1993*]. Moreover, in addition to the submarine permafrost layer, other substantial confining units may exist within the self sediments (as is suggested in the review by *Bratton [2010]*), increasing the complexity of flow. Furthermore, the groundwater discharge rates were held constant for each simulation until the system reached a quasi steady state; however, the discharge rate probably changes over the course of a single glacial cycle, or across several glacial cycles. Because of the long response times, the system is likely not sensitive to small- or high-frequency changes, but future studies should investigate the response to transient freshwater input and glacial cycles of both 41 and 100 ka periods. While we did not explicitly model hydrate deposits, their presence would alter sediment permeability. If the permeability changes are large, hydrate deposits may affect flow patterns as significantly as the permafrost layer does.

6. Conclusion

In this study, we investigate the role of terrestrial submarine groundwater discharge on the temperature and salinity field and its effect on the present-day extent of submarine permafrost offshore and gas hydrate stability on the Beaufort Shelf with a two-dimensional numerical model based on the finite volume method. This study finds that submarine groundwater discharge may play a large role in submarine permafrost evolution and gas hydrate stability and suggests that local hydrology may control the evolution of submarine permafrost as strongly as sea level variations, or air temperature. Permafrost evolution shows transient behavior over a potentially long time scale (e.g., several glacial cycles) before a balance of density

and pressure-driven flows is established with the permeability variations imposed by the overlying permafrost layer. The quasi-stationary location of the saltwater-freshwater transition is related to the detectable permafrost extent offshore. Larger values of groundwater discharge may allow permafrost to extend farther offshore because fresh pore water preserves relict ice. Therefore, differences in the permafrost extent at locations that share similar paleoclimatic history may be explained by differences in the local hydrology. Moreover, gas hydrate stability on the Beaufort Shelf may be more widespread than currently thought because low-ice saturation, highly degraded permafrost likely exists beyond the permafrost boundary detectable by common geophysical methods. While this study captures several physical behaviors not accounted for in similar modeling efforts (i.e., buoyancy-driven flows, heat and solute transport by advection, and long time scales), it is by no means physically complete or exhaustive. We hope this study, which demonstrates the important role of submarine groundwater discharge in circum-Arctic continental shelf processes, sparks further interest in the Arctic and gas hydrate community.

Acknowledgments

This study is supported by funding from the National Research Council Methane Hydrate Fellowship administered by the Department of Energy and the National Academies of Sciences. We thank Jerry Mitrovica for kindly providing the site-specific relative sea level curve used in this study and the comments from several peer reviewers which have helped improve this manuscript. For data supporting this numerical study, contact the corresponding author, Jennifer M. Frederick, jenn@dri.edu.

References

- Andler, P. M., and H. Brenner (1988), Multiphase flow in porous media, *Annu. Rev. Fluid Mech.*, 20, 35–59.
- Barenbaum, A. A. (2007), On possible relationship between gas hydrates and submarine groundwater, *Water Res.*, 34(5), 587–592.
- Belanger, A. M. (2007), Fluid flow in the central North Slope foreland basin, Alaska, Thesis dissertation, 50 pp., Louisiana State Univ., Baton Rouge.
- Blasco, S., et al. (2013), 2010 State of knowledge: Beaufort Sea seabed geohazards associated with offshore hydrocarbon development, *Geological Survey of Canada Open File*, 6989, 340, doi:10.4095/292616.
- Bratton, J. F. (2010), The three scales of submarine groundwater flow and discharge across passive continental margins, *J. Geol.*, 118(5), 565–575.
- Brothers, L. L., P. E. Hart, and C. D. Ruppel (2012), Minimum distribution of subsea ice-bearing permafrost on the U.S. Beaufort Sea continental shelf, *Geophys. Res. Lett.*, 39, L15501, doi:10.1029/2012GL052222.
- Cohen, D., et al. (2010), Origin and extent of fresh paleowaters on the Atlantic continental shelf, USA, *Groundwater*, 48(1), 143–158.
- Collett, T. S., and K. Bird (1993), Unfrozen, high-salinity intervals within icebearing permafrost, North Slope of Alaska, *6th Int. Conf. Permafrost*, Beijing.
- Collett, T. S. (1994), Permafrost-associated gas hydrate accumulations, *Ann. N.Y. Acad. Sci.*, 715, 247–269.
- Collett, T. S., M. W. Lee, W. F. Agena, J. J. Miller, K. A. Lewis, M. V. Zyrianova, R. Boswell, and T. L. Inks (2011), Permafrost-associated natural gas hydrate occurrences on the Alaska North Slope, *Mar. Pet. Geol.*, 28, 279–294.
- Dallimore, S. R., and T. S. Collett (1995), Intrapermafrost gas hydrates from a deep core hole in the Mackenzie Delta, Northwest Territories, Canada, *Geology*, 23(6), 527–530.
- Delisle, G. (1998), Temporal variability of sub-sea permafrost and gas hydrate occurrences as function of climate change in the Laptev Sea, Siberia, *Polarforschung*, 68, 221–225.
- Deming, D., J. H. Sass, A. H. Lachenbruch, and R. F. De Rito (1992), Heat flow and subsurface temperature as evidence for basin-scale ground water flow, North Slope of Alaska, *Geol. Soc. Am. Bull.*, 104(5), 528–542.
- de Roo, J. L., C. J. Peters, R. N. Lichtenhaler, and G. A. M. Diepen (1983), Occurrence of methane hydrate in saturated and unsaturated solutions of sodium chloride and water in dependence of temperature and pressure, *AIChE J.*, 29(4), 651–657.
- Dzyuba, A. V., and I. S. Zektser (2013), Variations in submarine groundwater runoff as a possible cause of decomposition of marine methane hydrates in the Arctic, *Water Res.*, 40(1), 74–83.
- Fofonoff, P., and R. C. Millard, Jr. (1983), Algorithms for the computation of fundamental properties of seawater, *UNESCO Technical Paper in Marine Science*, 44, 1–55.
- Frederick, J. M., and B. A. Buffett (2014), Taliks in relict submarine permafrost and methane hydrate deposits: Pathways for gas escape under present and future conditions, *J. Geophys. Res. Earth Surf.*, 119, 106–122, doi:10.1002/jgrf.20192.
- Frederick, J. M., and B. A. Buffett (2013), Use of cosmogenic 129-I to constrain numerical models of fluid flow in marine sediments: Application to the Blake Ridge Hydrate Province, *Geochim. Geophys. Geosyst.*, 14, 1343–1357, doi:10.1002/ggge.20059.
- Gwiazda, R., C. K. Paull, S. Dallimore, H. Mellings, and Y. K. Jin (2014), Distinctive sources of fluids in different environments of the Beaufort Sea seafloor, Abstract OS12A-06 presented at 2014 Fall Meeting, AGU, San Francisco, Calif., 15–19 Dec.
- Hanor, J. S., J. A. Nunn, and Y. Lee (2004), Salinity structure of the central North Slope foreland basin, Alaska, USA: Implications for pathways of past and present topographically driven regional fluid flow, *Geofluids*, 4, 152–168.
- Hatlelid, W. G., and J. R. MacDonald (1982), Permafrost determination by seismic velocity analyses, *J. Can. Soc. Explor. Geophys.*, 18(1), 14–22.
- Hu, K., D. R. Issler, Z. Chen, and T. A. Brent (2013), Permafrost investigation by well logs, and seismic velocity and repeated shallow temperature surveys, Beaufort-Mackenzie Basin, *Geological Survey of Canada Open File* 6956.
- Johansen, T. A., P. Digranes, M. V. Schaack, and I. Lonne (2003), On seismic mapping and modeling of near-surface sediments in polar areas, *Geophysics*, 68(2), 1–8.
- Judge, A. S., A. E. Taylor, M. Burgess, and V. S. Allen (1981), Canadian geothermal data collection-northern wells 1978–80, *Earth Physics Branch, EMR Canada, Geothermal Series* 12.
- Judge, A. S., and J. A. Majorowicz (1992), Geothermal conditions for gas hydrate stability in the Beaufort-Mackenzie area: The global change aspect, *Palaeogeogr. Palaeoclimatol. Palaeoecol.*, 98, 251–263.
- Kassens, H., H. Bauch, S. Drachev, A. Gierlich, F. Niessen, E. Taldenkova, A. Rudoi, J. Thiede, and M. Wessels (2000), The TRANSDRIFT VIII Expedition to the Laptev Sea: The Shelf Drilling Campaign of "Laptev Sea System 2000", Sixth Workshop on Russian-German Cooperation: Laptev Sea System 2000. October 12–14, 2000, St. Petersburg, Russia.
- Kendall, R. A., J. X. Mitrovica, and G. A. Milne (2005), On post-glacial sea level—II. Numerical formulation and comparative results on spherically symmetric models, *Geophys. J. Int.*, 161, 679–706.
- King, M. S., B. I. Pandit, J. A. Hunter, and M. Gajtani (1982), Some seismic, electrical, and thermal properties of sub-seabottom permafrost from the Beaufort Sea, *Proc. 4th Can. Permafrost Conf.*, 268–273.

- King, M. S., B. I. Pandit, R. W. Zimmerman, and R. F. Corwin (1988), Seismic and electrical properties of unconsolidated permafrost, *Geophys. Prospect.*, 36, 349–364.
- Kooi, H., and J. Groen (2000), Modes of seawater intrusion during transgressions, *Water Resour. Res.*, 36(12), 3581–3589.
- Lide, D. R. (ed.) (2013–2014), *CRC Handbook of Chemistry and Physics*, 94th ed., CRC Press, Boca Raton, Fla.
- Lisiecki, L. E., and M. E. Raymo (2005), A Pliocene-Pleistocene stack of 57 globally distributed benthic $\delta^{18}\text{O}$ records, *Paleoceanography*, 20, PA1003, doi:10.1029/2004PA001071.
- Matsumoto, R., H. Tomaru, Y. F. Chen, H. Lu, and I. D. Clark (2005), Geochemistry of the interstitial waters of the JAPEX/JNOC/GSC et al Mallik 5L-38 gas hydrate production research well, *GSC Bull.*, 585, 98–99.
- Mavko, G., and A. Nur (1997), The effect of a percolation threshold in the Kozeny-Carman relation, *Geophysics*, 62, 1480–1482.
- Moore, W. S. (2010), The effect of submarine groundwater discharge on the ocean, *Annu. Rev. Mar. Sci.*, 2, 59–88, doi:10.1146/annurev-marine-120308-081019.
- Nicol'sky, D. J., and N. E. Shakhova (2010), Modeling sub-sea permafrost in the East Siberian Arctic Shelf: The Dmitry Laptev Strait, *Environ. Res. Lett.*, 5, 0115006, doi:10.1088/1748-9326/5/1/015006.
- Nicol'sky, D. J., V. E. Romanovsky, N. N. Romanovskii, A. L. Kholodov, N. E. Shakhova, and I. P. Semiletov (2012), Modeling sub-sea permafrost in the East Siberian Arctic Shelf: The Laptev Sea region, *J. Geophys. Res.*, 117, F03028, doi:10.1029/2012JF002358.
- Osterkamp, T. E., G. C. Baker, W. D. Harrison, and T. Matava (1989), Characteristics of the active layer and shallow subsea permafrost, *J. Geophys. Res.*, 94(C11), 16,227–16,236.
- Osterkamp, T. A. (2001), Sub-sea permafrost, in *Encyclopedia of Ocean Sciences*, pp. 559–569, Academic Press.
- Paull, C. K., W. Ussler III, S. R. Dallimore, S. M. Blasco, T. D. Lorenson, H. Melling, B. E. Medioli, F. M. Nixon, and F. A. McLaughlin (2007), Origin of pingo-like features on the Beaufort Sea shelf and their possible relationship to decomposing methane gas hydrates, *Geophys. Res. Lett.*, 34, L01603, doi:10.1029/2006GL027977.
- Paull, C. K., et al. (2011), Tracking the decomposition of submarine permafrost and gas hydrate under the shelf and slope of the Beaufort Sea, *Proc. 7th Int. Conf. on Gas Hydrates*, Edinburgh, Scotland, 17–21 July.
- Peltier, W. R. (2004), Global glacial isostasy and the surface of the ice-age Earth: The ICE-5G (VM2) Model and GRACE, *Annu. Rev. Earth Planet. Sci.*, 32, 111–149.
- Petit, J. R., et al. (1999), Climate and atmospheric history of the past 420,000 years from the Vostok Ice Core, Antarctica, *Nature*, 399, 429–436.
- Petit, J. R., et al. (2001), *Vostok Ice Core Data for 420,000 Years, IGBP PAGES/World Data Center for Paleoclimatology Data Contribution Series #2001-076*, NOAA/NGDC Paleoclimatology Program, Boulder, Colo.
- Phrampus, B. J., M. J. Hornbach, C. D. Ruppel, and P. E. Hart (2014), Widespread gas hydrate instability on the upper U.S. Beaufort margin, *J. Geophys. Res. Solid Earth*, 119, 8594–8609, doi:10.1002/2014JB011290.
- Pohlman, J., T. D. Lorenson, P. E. Hart, C. D. Ruppel, C. Joseph, M. E. Torres, and B. D. Edwards (2011), Abstract GC41B-0813 presented at 2011 Fall Meeting, AGU, San Francisco, Calif, 5–9 Dec.
- Pohlman, J., C. Ruppel, C. Maue, L. Brothers, J. Kessler, and C. Worley (2012), Real-time mapping of seawater and atmospheric methane concentrations offshore of Alaska's North Slope, *USGS Sound Waves*, 140, 4–5.
- Portnov, A., A. J. Smith, J. Mienert, G. Cherkashov, P. Rekant, P. Semenov, P. Serov, and B. Vanshtain (2013), Offshore permafrost decay and massive seabed methane escape in water depths > 20 m at the South Kara Sea shelf, *Geophys. Res. Lett.*, 40, 3962–3967, doi:10.1002/grl.50735.
- Portnov, A., J. Mienert, and P. Serov (2014), Modeling the evolution of climate-sensitive Arctic subsea permafrost in regions of extensive gas expulsion at the West Yamal shelf, *J. Geophys. Res. Biogeosci.*, 119, 2082–2094, doi:10.1002/2014JG002685.
- Post, V. E. A., and H. Kooi (2003), Rates of salinization by free convection in high-permeability sediments: Insights from numerical modeling and application to the Dutch coastal area, *Hydrogeol. J.*, 11, 549–559.
- Post, V. E. A., J. Groen, H. Kooi, M. Person, S. Ge, and W. M. Edmunds (2013), Offshore fresh groundwater reserves as a global phenomenon, *Nature*, 504, 71–78, doi:10.1038/nature12858.
- Rachold, V., D. Y. Bolshiyanov, M. N. Grigoriev, H.-W. Hubberten, R. Junker, V. V. Kunitsky, F. Merker, P. Overduin, and W. Schneider (2007), Nearshore Arctic subsea permafrost in transition, *Eos Trans. AGU*, 88(13), 149–156, doi:10.1029/2007EO130001.
- Romanovskii, N. N., H. W. Hubberten, A. V. Gavrilov, A. A. Eliseeva, and G. S. Tipenko (2005), Offshore permafrost and gas hydrate stability zone on the shelf of East Siberian Seas, *Geo-Mar. Lett.*, 25, 167–182.
- Ruppel, C. D. (2011), Methane hydrates and contemporary climate change, *Nat. Educ. Know.*, 3(10), 29.
- Ruppel, C. D., J. Pohlman, M. P. Woo, M. Casso, P. Hart, and L. Brothers (2013), Methane fluxes from the Western Arctic Ocean: No evidence for an Arctic methane catastrophe, *Final PERGAMON Symposium*, GEOMAR Center for Ocean Research, Kiel, Germany, 5–7 Nov.
- Sellmann, P., and E. Chamberlain (1980), Permafrost beneath the Beaufort Sea: Near Prudhoe Bay, Alaska, *J. Energy Res. Technol.*, 102, 35–48.
- Schlitzer, R. (2014), Ocean data view. <http://odv.awi.de>, Accessed 04/25/2014.
- Shakhova, N., et al. (2013), Ebullition and storm-induced methane release from the East Siberian Arctic Shelf, *Nat. Geosci.*, 7, 64–70.
- Smith, S. L., and A. S. Judge (1993), Gas hydrate database for Canadian Arctic and selected east coast wells: Geological Survey of Canada Open File Report 2746.
- Taniguchi, M., W. C. Burnett, J. E. Cable, and J. V. Turner (2002), Investigation of submarine groundwater discharge, *Hydrol. Processes*, 16, 2115–2129.
- Taylor, A. E., S. R. Dallimore, and S. I. Outcalt (1996a), Late Quaternary history of the Mackenzie-Beaufort region, Arctic Canada, from modelling of permafrost temperatures: I. The onshore-offshore transition, *Can. J. Earth Sci.*, 33, 52–61.
- Taylor, A. E., S. R. Dallimore, and A. S. Judge (1996b), Late Quaternary history of the Mackenzie-Beaufort region, Arctic Canada, from modelling of permafrost temperatures. 2. The Mackenzie Delta-Tuktoyaktuk Coastlands, *Can. J. Earth Sci.*, 33, 62–71.
- Taylor, A. E., S. R. Dallimore, P. R. Hill, D. R. Issler, S. Blasco, and F. Wright (2013), Numerical model of the geothermal regime on the Beaufort Shelf, arctic Canada since the Last Interglacial, *J. Geophys. Res. Earth Surf.*, 118, 2365–2379, doi:10.1002/2013JF002859.
- Torres, M. E., T. S. Collett, K. K. Rose, J. C. Sample, W. F. Agena, and E. J. Rosenbaum (2011), Pore fluid geochemistry from the Mount Elbert Gas Hydrate Stratigraphic Test Well, Alaska North Slope, *Mar. Pet. Geol.*, 28, 332–342.
- Weaver, J. S., and J. M. Stuart (1983), In situ hydrates under the Beaufort Sea shelf, *Proc. 4th Can. Permafrost Conf.*, Fairbanks, Alaska, 18–22 July.
- Williams, J. R. (1970), Ground water in the permafrost regions of Alaska, *USGS Professional Paper*: 696.
- World Ocean Database (WOD) (2009), *Ocean Climate Laboratory/National Oceanographic Data Center/NESDIS/NOAA/U.S. Department of Commerce*, World Ocean Database and World Ocean Atlas, Research Data Archive at the National Center for Atmospheric Research, Computational and Information Systems Laboratory, Boulder, Colo.